Strong Quenching of Dye Fluorescence in Monomeric Perylene Orange/TMDC Hybrid Structures

Supporting Information

Tim Völzer[a,b], Alina Schubert[a,b], Erik von der Oelsnitz[a,b], Julian Schröer[a,b], Ingo Barke[a,b], Rico Schwartz[a], Kenji Watanabe[c], Takashi Taniguchi[d], Sylvia Speller[a,b], Tobias Korn[a,b], and Stefan Lochbrunner[a,b,*]

a) Institute of Physics, University of Rostock, Albert-Einstein-Str. 23, 18059 Rostock, Germany

b) Department "Life, Light and Matter", University of Rostock, Albert-Einstein-Str. 25, 18059 Rostock, Germany

c) Research Center for Electronic and Optical Materials, National Institute for Materials Science, 1-1 Namiki, Tsukuba 305-0044, Japan

d) Research Center for Materials Nanoarchitectonics, National Institute for Materials Science, 1-1 Namiki, Tsukuba 305-0044, Japan

*stefan.lochbrunner@uni-rostock.de

Contents

1 Coating techniques for the preparation of hybrid structures

1.1 Thermal vapor deposition at different temperatures

In the experimental section of the main body of the manuscript, we presented the optimal, standard procedure to create hybrid structures via thermal vapor deposition (TVD). Nevertheless, going beyond this optimum can provide insight in the limits of this preparation technique and how to recognize them. The most relevant parameter for TVD lies in the temperature, determining the evaporation rate of the coating substance as well as the kinetic energy of the molecules hitting the target. Therefore, we varied this parameter to investigate its influence on the absorption and emission spectra of the resulting perylene orange (PO) layer as well as to find the optimum value for monomer coating. Here, we remark that the optimum evaporation temperature may vary by several $10\,\mathrm{K}$ depending on the exact amount and distribution of the dye powder in the reservoir, plus the thermal contact at the different interfaces of the setup.

In different coating procedures, the temperature of the PO powder was tuned from 440 to $470\,\mathrm{K}$. Each sample was coated for $40\,\mathrm{min}$ including the heating up. As they were performed consecutively in one series, the heating block with the dye powder never started at room temperature but was still warm from the previous run. The resulting absorption and emission spectra are depicted in Figure S1. For the absorption, we observe a prominent multi-peak structure resulting from the Frank-Condon progression, that remains essentially constant in shape for all regarded evaporation temperatures. Merely the amplitude rises with increasing temperature, as more molecules are evaporated in the same time span. The emission spectra also exhibit the monomer-related multi-peak structure at low evaporation temperature that indicates the presence of monomer PO. At higher evaporation temperatures, the first thing to change is the fluorescence intensity rising. Afterwards, the 0-0 peak shrinks, while the broad emission band at the long-wavelength tail of the spectrum emerges. This contribution is likely caused by the formation of aggregates[1] or nanocrystals[2,3] that support excimer emission. While the absorption is still governed by single molecules, the energy is then transferred to the lower-lying excimer state that eventually emits[4,5], typically with a broad red-shifted fluorescence band[6]. Upon raising the evaporation temperature even further up to roughly $470\,\mathrm{K}$, three separate peaks form anew, although their weighting differs from the monomer situation. Here, the 0-2-peak seems strongest, which may possibly indicate the presence of further aggregate
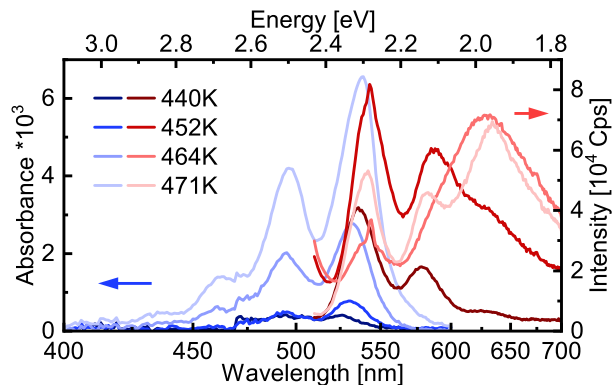

Figure S1: Absorption and emission spectra of TVD PO films in dependence of the evaporation temperature. In contrast to the absorption simply growing with increasing temperature and maintaining its multi-peak structure, as more molecules evaporate, the behavior of the emission involves a higher degree of complexity. First, the signal rises, roughly keeping its shape. From 452 to $464\,\mathrm{K}$, the already discussed broad emission band emerges, parallel to the 0-0-peak shrinking. A further temperature increase, however, leads to a recovery of the multi-peak structure, albeit with a higher weighting of the low-energy signatures.

states, accessible due to the higher kinetic energy of the evaporated molecules.[6]

1.2 Estimation of dye coverage

Based on the absorption strength of the optimal monomer film, as discussed in section 1.1, we are able to calculate the molecular coverage after TVD with standard parameters. We take an absorbance value of $A = 0.5 \cdot 10^{-3}$ for the 0-0-peak of the optimal monomer coating (see Figure S1) and an extinction coefficient for PO of $\varepsilon = 8.5 \times 10^4\,\text{M}^{-1}\,\text{cm}^{-1} = 8.5 \times 10^7\,\text{cm}^2\,\text{mol}^{-1}$ measured in chloroform solution[7]. Lambert-Beer's law constitutes the relation between the absorbance and the areal molecular density ϱ as follows:

$$A = \varepsilon_{\text{eff}} \cdot c \cdot l = \varepsilon_{\text{eff}} \cdot \varrho \tag{1}$$

with the concentration c and the path length l through the medium. ε_{eff} denotes the effective extinction coefficient. It differs from the one in solution, as we assume a flat orientation of the molecules on the surface (x- and y-direction). For PO, the transition dipole moment $\vec{M}$ lies parallel to the longer symmetry axis, i.e. in-plane[8]. Consequently, the mean orientation of $\vec{M}$ and the electric field $\vec{E}$ is advantageous compared to a random distribution. This results in a higher absorbance, scaling with $A \propto |\vec{M} \cdot \vec{E}|^2$. To quantify this effect, we calculate the normalized mean squared projection q of $\vec{M}$ onto $\vec{E}$, with the latter being fixed parallel to the x-axis - for perpendicular incidence, i.e. z-direction light beam and with no loss of generality. In the following, we use spherical coordinates, yielding $\frac{|\vec{M} \cdot \vec{E}|}{|\vec{M}| \cdot |\vec{E}|} = \cos\varphi \cdot \sin\theta$.

For a random orientation as in solution, we obtain:

$$q_{\text{random}} = \frac{\int_0^{2\pi} \int_0^{\pi} (\cos^2\varphi \cdot \sin^2\theta) \sin\theta \, d\theta \, d\varphi}{\int_0^{2\pi} \int_0^{\pi} \sin\theta \, d\theta \, d\varphi} = \frac{1}{3} \tag{2}$$

stating an attenuation of the absorption by a factor of three in random orientation versus perfect parallel alignment of transition dipole moment and electric field. Analogously, in-plane orientation of the molecules (i.e. $\theta = \frac{\pi}{2}$) results in

$$q_{\text{in-plane}} = \frac{\int_0^{2\pi} \cos^2\varphi \, d\varphi}{\int_0^{2\pi} d\varphi} = \frac{1}{2} \tag{3}$$

In terms of extinction coefficients, this constitutes the relation:

$$\frac{\varepsilon_{\text{eff}}}{\varepsilon} = \frac{q_{\text{in-plane}}}{q_{\text{random}}} = \frac{3}{2} \tag{4}$$

Hence, the face-down orientation of the molecules on the surface manifests in a 1.5-fold higher absorption per molecule compared to the value measured in solution.

Returning to Lambert-Beer's law (Equation (1)), this yields a areal molecule density of roughly

$$\varrho = \frac{2A}{3\,\varepsilon} \approx 2.4 \times 10^{-2}\,\text{nm}^{-2} \equiv 2.4 \times 10^{12}\,\text{cm}^{-2} \tag{5}$$

corresponding to an area of about $42\,\text{nm}^2$ per molecule, i.e. roughly $\frac{1}{30}$ of a perfect dye monolayer, and a mean molecular distance of $6.5\,\text{nm}$ compared to a molecule size of $0.7\,\text{nm} \times 2\,\text{nm}$. These values clearly confirm the monomer nature of the PO coating.

1.3 Inhomogeneities and quenching on stamp-coated 1L-TMDCs

As an alternative viable method for the deposition of molecules onto a target substrate, we tested stamping. Initially, the viscoelastic polydimethylsiloxane (PDMS) stamp is spin-coated
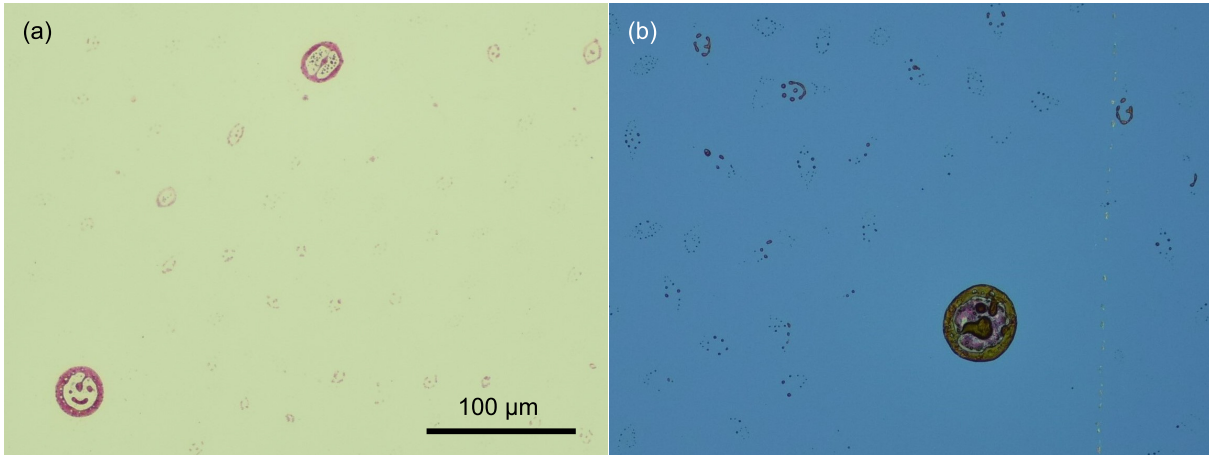
Figure S2: Stamp-coating of perylene orange. (a) Micrograph of a spin-coated PDMS stamp. The dye agglomerates on several spots to form clearly visible structures with a size of up to 50 μm as well as a variety of smaller spots. In between these accumulation centers, preferably in the vicinity of large structures, areas without visible inhomogeneities exist. (b) Microscope image of a stamp-coated Si/SiO$_2$ wafer. Here, the same structures as on the PDMS occur, suggesting a high transfer yield. Aiming a agglomerate-free region at the target flake during the stamping facilitates monomer coating.

with a 900 μM solution of PO in chloroform. Afterwards, the dye is transferred to the target by stamping, similar to the deterministic transfer of 2D flakes[9]. However, as the PDMS has a rather rough surface and the solution is quite concentrated, many spots of agglomerated PO form during the spin-coating, which will also transfer to the target substrate, see Figure S2. To avoid stamping such an agglomerate onto the flake of interest, one has to aim between those spots, where the molecule coverage is typically homogeneous. This can be monitored by an optical microscope commonly implemented in such stamping setups. Nevertheless, some
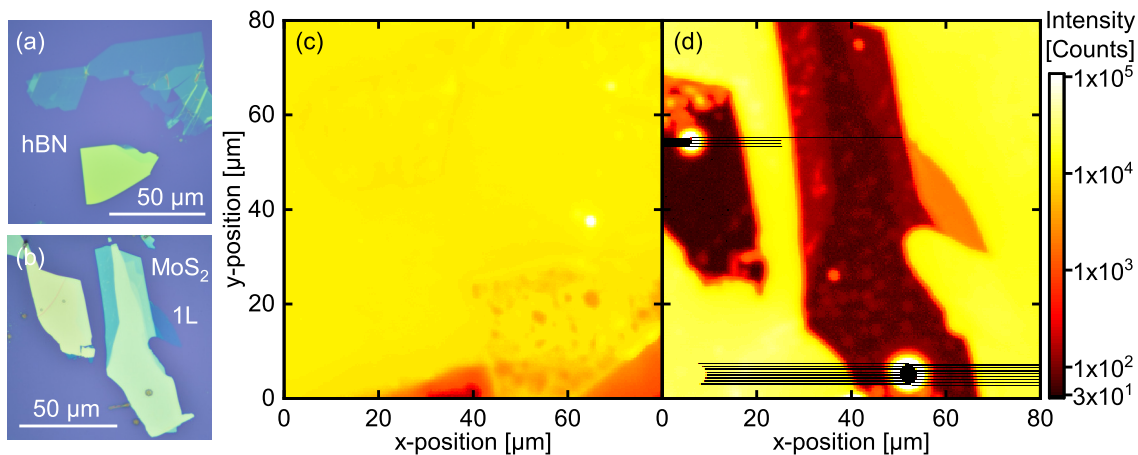

Figure S3: FLIM measurements of 2D crystals stamped with PO. No additional band pass filter was used in these experiments (a, b) Micrographs of hBN and MoS$_2$ flakes on wafer substrates, respectively. (c) FLIM intensity map of the hBN crystals depicted in (a). The intensity is homogeneous over the vast majority of the area. The only exceptions are two bright spots on the right and in the top right corner as well as the dark bottom right one, where the contact between PDMS and substrate ended. (d) FLIM intensity map of the MoS$_2$ crystals depicted in (b). While the intensity exhibits a constant level on the substrate, it drastically falls on the TMDC flakes. Exceptions occur with the two prominent bright spots on the flakes, which probably result from dye agglomerates. Here, the high emission intensities trigger a safety shutter in front of the FLIM detector for several seconds, blocking the incoming light and leading to the dark horizontal lines.

4

small (sub-)micron agglomerates may be barely visible, yet exhibiting much higher fluorescence signals than the monomer-coated environment, as the results from fluorescence lifetime imaging microscopy (FLIM) in Figure S3 (d) show. This leaves a small risk of accidentally putting a small agglomerate onto the flake of interest, creating an inhomogeneous coating.

Apart from these preparational shortcomings, the stamping method is able to reproduce the findings regarding the quenching observed on samples coated by thermal vapor deposition (TVD). Figure S3 presents the fluorescence lifetime imaging microscopy (FLIM) intensity maps for stamp-coated hBN and MoS_2 flakes. Analogously to the TVD samples, the hBN regions exhibit an intensity level similar to the wafer surroundings, while the MoS_2 crystals show a strong contrast, with the fluorescence dropping by up to three orders of magnitude compared to their environment. Note that no additional band pass filter was used in these measurements. Consequently, we observe extraordinarily bright spots that match the dye agglomerates, for instance when comparing Figure S3 (b) and (d). On top of that, the monolayer MoS_2 photoluminescence causes the respective area to stand out from the other flake regions, as it also happens in section 4.4. Thus, a quantitative analysis of the quenching as well as the time-resolved signal does not appear reasonable at this point. Nevertheless, the occurrence of strong quenching becomes evident in this case as well, supporting the findings from the main body, section "Rapid fluorescence quenching in TMDC hybrids".

2 Photodegradation of PO at ambient conditions

Since PO is prone to photooxidation[10], all measurements were performed either in vacuum or by applying only short illumination times to avoid degradation of the molecule film. To quantify the severity of this issue, we performed degradation measurements in the microscopic emission spectroscopy setup, in this case under ambient conditions. Omitting the cryostat with its glass window in the laser beam, we obtained a slightly smaller focal diameter of roughly 1 µm. On top of that, we doubled the excitation power to 10 µW at 532 nm. In sum, we applied an about four-fold intensity compared to the measurements under vacuum that were discussed in the main
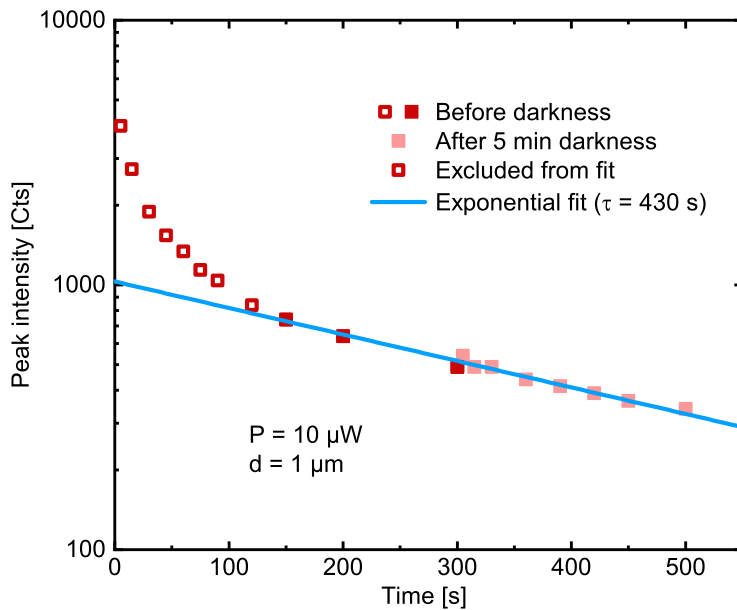

Figure S4: Photodegradation of PO on wafer substrate under ambient conditions. Following a non-monoexponential decay within the first 2 min, the intensity decreases exponentially, as indicated by the fit. During the 5 min of darkness, no substantial recovery of the signal is observed, suggesting a non-reversible degradation of the dye molecules.

body. We chose a spot on the wafer substrate, far from any flakes and monitored the emitted intensity of the 0-0-peak over time. The resulting signal evolution is presented in Figure S4. First, we observed a drastic signal decay by a factor of five within the first two minutes, which does not follow a simple exponential behavior. Afterwards, the curve evolves into a monoexponential signal reduction. After 5 min, we blocked the laser beam for the same duration, to check whether any recovery mechanism is present. However, no substantial increase of the signal was observed after 5 min of darkness, suggesting that the degradation is permanent. The exponential decay, on the other hand, continues at the same rate. A corresponding fit yielded a time constant of about 400 s. All in all, these findings demonstrate the importance of avoiding photooxidation during the measurements, as especially freshly prepared dye films lose a significant amount of intensity within a short time.

3 AFM measurements

Now that we established suitable preparation approaches, with the macroscopic optical spectra pointing to monomer characteristics of the deposited molecules, we strive for a structural characterization of the samples by atomic force microscopy (AFM). This ought to reveal or exclude the formation of larger supramolecular structures as well as to determine the flake and film thickness and homogeneity, even though molecular resolution lies beyond the scope of this work. AFM measurements were conducted in ambient (Park XE-100) using silicon cantilevers (SSS-NCHR, Nanosensors) and dynamic mode. Excitation frequencies slightly larger than the fundamental eigenfrequency and constant-amplitude set points between 65 % and 80 % of the free amplitude were chosen. Data analysis was done using Gwyddion[11] and Igor Pro (Wavemetrics, Inc.). For background correction, a linewise linear function as well as a 2D plane were subtracted. We chose a few-layer WSe_2 and hBN flake, exfoliated and transferred to a Si/SiO_2 wafer, respectively. They were annealed at 550 K and 4×10^{-4} mbar for 20 h, to desorb water and other physisorbed species, and obtain a largely clean surface for the AFM measurements. We investigated the blank samples before and after TVD coating and again five months afterwards. Note that in contrast to the standard procedure, we kept the samples in the evacuated TVD chamber at 3×10^{-5} mbar and room temperature over the weekend (2.7 days) before starting the actual coating process by heating up the dye reservoir. This ought to maintain a relatively clean sample surface, yet it might have an influence on the vapor deposition, as the lower pressure may cause a higher evaporation rate of the dye powder and the transport regime from reservoir to sample probably changed from diffusive to ballistic. On top of that, the desorption of other adsorbates may influence the mobilty of the PO molecules on the respective substrates. As a complement to the AFM measurements, we performed FLIM and micro-photoluminescence (µ-PL) spectroscopy on the same flakes to obtain correlative data.

The AFM analyses show clear differences in the sample topographies, induced by the dye molecule deposition, see Figure S5 (a), (b), (d) and (e). As the highest structures, we observe 3D molecular agglomerates that form exclusively on the substrate and not on the crystal flakes. They measure about 200 nm in diameter and 40 nm in height, exhibit an oblate shape and also appear in FLIM scans without the band pass filter as resolution-limited bright dots, as shown in Figure S5 (c). If converted into a homogeneous coating, these agglomerates correspond to a coverage of about 1 Å in height, i.e. about one third of a perfect monolayer of in-plane oriented flat PO molecules. In between the dots, however, a homogeneous residual fluorescence intensity is detected, pointing to a uniform molecule coverage aside from the 3D aggregates, compatible with a Stranski-Krastanov growth mode[12].

In a zone of $3 - 5$ µm around the flakes, however, no agglomerates are present and the areal fluorescence intensity is significantly reduced, suggesting a depletion of molecules, which are drawn towards the flakes. This assumption is confirmed by the change of the flake edge height due to PO coating, visible in the AFM line profiles in Figure S5 (f). While the thinnest regions

of the blank hBN and WSe$_2$ size to $h = 7$ and $4\,\mathrm{nm}$ in edge height, i.e. about twenty[13] and six[14–16] layers, they rise by about $\Delta h = 1.5\,\mathrm{nm}$ $(15 - 25\,\%)$ and $4\,\mathrm{nm}$ $(90 - 100\,\%)$ upon molecule deposition, respectively. These values lie well beyond the calculated average molecule coverage on the remote substrate regions. Although the growth of the step height is accompanied by the emergence of PO fluorescence in the hBN flake area drastically exceeding the intensity on the substrate, no indications of larger structures of PO molecules on the crystal surface were found. Thus, we conclude a migration of the molecules below the flake.

Generally, when molecular species are deposited on surfaces with weak interaction, such as van-der-Waals crystals, their diffusion is high. Nevertheless, for the most part, after minutes to hours, molecular assemblies are formed. This can proceed via 2D surface "gas" over a liquid phase towards crystalline aggregates, on graphite[17] or graphene[18] surfaces. Only occasionally, persistence of the 2D gas of monomers or dimers or the liquid phase is observed. Examples are benzene on Cu(111) at $77\,\mathrm{K}$[19], fluorinated copper phthalocyanine on Si(111)/Tl-(1×1)[20] and 2,5-dihydroxybenzoic acid (DHBA) molecules on calcite[21]. In our case, the PL spectrum of the PO in the hBN region features only a small contribution of monomer PO and is instead dominated by a broad low-energy band that occurs exclusively in this sample (Figure S6 (b)), yet baring similarities to the emission of thicker PO coatings (for comparison, see SI sections 1.1 and 1.3). This suggests the presence of the dye molecules in some aggregated form with a broad
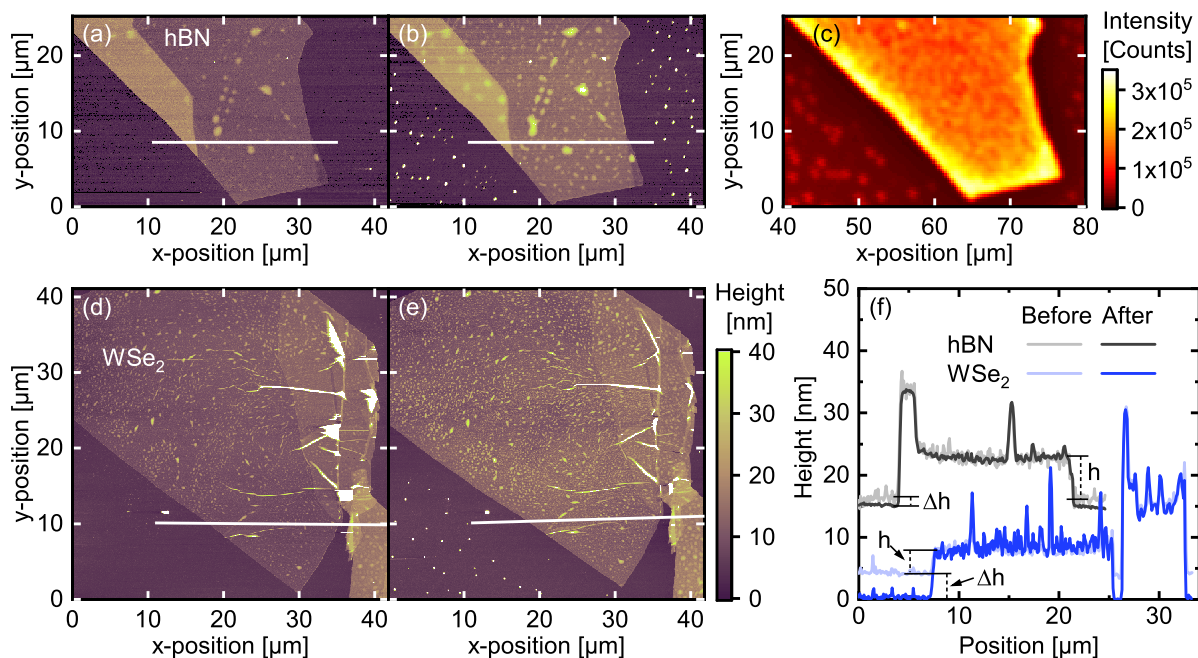

Figure S5: Topography of hybrid structures. Dynamic mode AFM height maps of hBN (a, b) and WSe$_2$ (d, e) before (a, d) and after (b, e) molecule deposition, respectively. Upon TVD, oblate dye agglomerates appear on the substrate surface, with a diameter of about $200\,\mathrm{nm}$ and an average height of $40\,\mathrm{nm}$. In a halo of several µm around the flake, however, these dots are missing. On the crystals, especially on the hBN, in contrast, already present blobs grow and new ones form. The white lines mark the positions, at which the line height profiles in (f) were taken. (c) FLIM intensity map of the area depicted in (a) and (b). On the substrate, the agglomerates show as bright spots, with a homogeneous intensity in between. The halo around the flake is characterized by a reduced fluorescence signal, while the flake area already stands out and its rim exhibits an even brighter emission. Other than that, no intensity variations occur in the crystal area that would match any of the AFM topography patterns. (f) Height profiles taken along the lines marked in (a, b, d, e), each averaged over a width of two pixels. hBN curves are offset for clarity. Note that the profiles after molecule deposition are shifted relatively to match the flake surface before the coating, respectively, demonstrating that the height increase is constant over the whole crystal area.

7

emission band, which is further red-shifted by the dielectric environment in that encapsulated situation[22].

If not residing at the surface, the two fundamental options for the molecules are either the deposition between the substrate and the hBN, lifting up the flake, or the intercalation between the individual crystal layers, ergo stretching the material in out-of-plane direction[23,24]. However, as the height increase during PO deposition is essentially independent of the original flake thickness and so is the FLIM intensity, we favor the first explanation. Nevertheless, minor contributions from intercalation cannot be excluded.

On top of that, inverse to the situation on the substrate, the fluorescence intensity on the hBN flake rises in the vicinity of the crystal edge and levels within about 5 µm into the interior. This provides another indication for the migration of the dye molecules from the exposed substrate to the cleft between wafer and flake. The lateral size of the dark depletion and bright accumulation zones represents the average diffusion length of the PO molecules. For the WSe$_2$ flake, in contrast, the strong fluorescence quenching, which is explicitly investigated in the following section, inhibits a comparison between FLIM intensities and AFM topographies.

PO is a relatively large aromatic molecule, such that in view of the literature[17,18], molecular assembly is expected at room temperature. Similar molecules normally do form crystals[2,25], while literature on PO assembly structure on graphite or similar surfaces is lacking, to our best knowledge. In our study, however, aggregates form exclusively on the Si/SiO$_2$ surface, but not on top of the hBN and WSe$_2$ flakes. As mentioned above, most of the molecules have migrated underneath the flakes. Yet, on the flake, we still observe signatures of mobile species and AFM error images sometimes indicate persistent amplitude instabilities. An option for explanation is a very dilute, residual 2D molecule gas, which essentially aggregated after months. The density of molecules on the flake is extremely low, and a large amount might have been captured by the tip and shaft, dynamically changing the tip-sample configuration.

All in all, these measurements demonstrate the strong relation between the configuration of the deposited molecules and the corresponding emission spectra. Any deviation from the monomeric character seems to result in definite spectral changes, distorting the multi-peak structure. Thus, we regard the Franck-Condon progression as a clear indicator for the presence of monomer dye molecules.

With respect to the agglomerates on the wafer substrate, both the AFM measurements and the FLIM intensity maps (without the band pass filter) show dots emerging after the PO deposition. The overlay of these two images (see Figure S6 (a)) demonstrates the matching of the agglomerates' positions, proving their identity. While the AFM topographies yielded a width of about 200 nm for these structures, the spatial resolution of nearly 1 µm determines their size in the FLIM maps. In measurements employing the band pass filter from 500 to 550 nm, however, no traces of these spots are found, suggesting their emission to be red-shifted relative to the 0-0-band of the monomer fluorescence or to be generally weaker due to their small area compared to the homogeneous monomer background. In the hBN area, where the FLIM intensity is drastically enhanced compared to the substrate, the µ-PL spectrum is dominated by a broad contribution, peaking around 650 nm. Although its shape bears striking similarities with the supposed excimer band of thicker coatings (see section 1), it exhibits a further red-shift compared to the latter. We assign this energetic shift to the complete encapsulation of the PO, leading to a different dielectric environment. When molecules are placed in contact with insulating layers, their gap between the highest occupied and lowest unoccupied molecular orbital (HOMO-LUMO gap, as measured by tunneling spectroscopy) can substantially shrink further than solely upon aggregation. For instance, individual pentacene placed on hBN/Rh(111) exhibits only 68 % of the original gap energy[22]. This gap reduction may originate from transient ionic states, i.e. positive- and negative-ion resonances assuming a Coulomb model and a dielectric hBN spacer with $\varepsilon_r = 4$. Alternatively, it could be explained qua vibration, if in the aggregate, higher vibrational states are present that get frustrated in the flake.
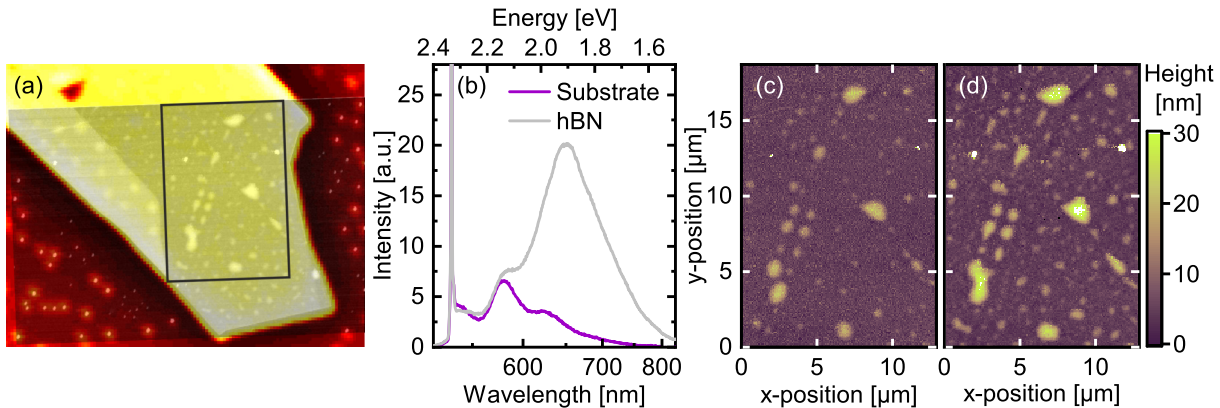
Figure S6: (a) Overlay of AFM topography (gray scale) and FLIM intensity map (fire color scale, logarithmic) of TVD-coated hBN flake, as already presented separately in Figure 3 (b) and (c). The positions of the "dots" on the substrate coincide for both images. The black rectangle marks the area depicted in (c) and (d). (b) µ-PL spectra of the different sample regions. While on the substrate, the spectrum remains similar to the monomer, it is dominated by a broad, low-energy contribution in the hBN region. This contribution is even red-shifted with respect to the excimer bands discussed in section 1.1. (c, d) AFM topography of the area marked in (a) before (c) and after (d) molecule deposition. The initially present blobs grow in height and area, some merge and even new ones are created.

On the 2D material flakes, we observe a growth in height at the crystal edges that – in case of the hBN – is accompanied by an enhanced fluorescence from the flake area with an even brighter region at the flake rim. We conclude the migration of molecules from the top and surrounding of the flakes into the cleft between flake and substrate. In other studies, however, height increases have been observed upon $200\,\mathrm{s}$ of irradiating WSe_2 flakes with a laser intensity of $5.1\,\mathrm{mW}$ at $532\,\mathrm{nm}$ focused through a 100x objective [16]. Here, the proposed explanation was photo-assisted formation of WO_3. In our case, in contrast, the FLIM was conducted after the first AFM measurements and excitation powers of only $12.5\,\mathrm{µW}$ were applied using a 20x objective. Hence, we exclude a photo-assisted oxidation as the cause for the growth of the flake heights.

In addition to the height increase at the flake edges, we observe blobs on the blank crystals that enlarge and in part even fuse, as depicted in Figure S6 (c) and (d). Since they are lacking phase contrast, we conclude that the respective material resides below the surface. Consequently, as the flake is locally elevated, they form a cavern that has to be supported by some material functioning as a pillar. Although we expect an accumulation of material, especially when the blobs grow during the PO deposition, no signs of an pronounced PO coverage is observed in the FLIM intensity maps of these regions. Ergo, we characterize these features as traps for adsorbed gases or other molecules, accumulating in the initially present blobs and thus contributing to their growth. This might have happened even before the dye molecule deposition during the evacuation of the TVD chamber.

4 Optical characterization

4.1 Multi-particle excitations at low temperatures

The charge of the trions observed in low-temperature measurements crucially determines the discussion about possible charge transfer and its direction in the PO/WSe$_2$ hybrid presented in the main body, Figure 3. To further investigate and distinguish the emission contributions, we performed µ-PL spectroscopy at 10 K. The resulting spectrum is shown in Figure S7.
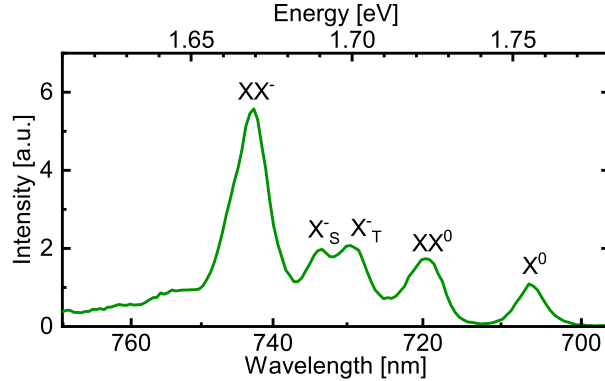

Figure S7: PL spectrum of PO/WSe$_2$ hybrid structure at 10 K. Several distinct peaks occur red-shifted from the neutral exciton emission (X^0). The double feature at around 1.7 eV is a characteristic of negative trions, while the remaining features are attributed to (charged) biexcitons. [26]

Following the trend of the measurements at room temperature and 80 K in Figure 3 of the main body, the WSe$_2$ emission is split up into multiple peaks, with the excitonic one as the energetically highest. Here, the occurrence of a double feature is a clear sign for negative trions, which subdivide into a singlet and triplet band. In contrast, the interpretation as well as the positions and relative distances of the remaining peaks vary in literature and supposedly depend strongly on the sample quality. [26–29]

From these results, we conclude that the WSe$_2$ flake is n-doped. Consequently, the additional PL peak at 80 K can be assigned to negative trions as well (see Figure 3 of the main body).

4.2 Agglomerate formation and dynamics on hBN3

To elucidate whether agglomeration effects play a role in the signal intensity and dynamics of the hBN1 and 2 samples, we TVD-coated the hBN3 sample with a higher molecular coverage, provoking the formation of dye agglomerates. Figure S8 (a) shows the corresponding FLIM intensity map, with bright spots on the hBN indicating the formation of agglomerates. Interestingly, this takes place only on the flake, while the intensity is equally distributed on the wafer substrate, as opposed to what was observed in the AFM measurements (chapter 3). We suppose the difference to originate from the long evacuation time in the preparation of the AFM samples. Without this, only the flat and inert hBN surface offers a mobility high enough for the molecules to meet each other to form larger structures, in contrast to the rough SiO$_2$ with its dangling bonds. however, when other adsorbates are largely removed before molecule deposition, the mobility is generally higher, allowing for agglomerate formation on the wafer. For the hBN, the dye mobility under this conditions is so high, that the molecules are able to migrate below the flake, as discussed before in section 3.

In the case of the hBN3 sample, we analyzed the temporal evolution of the fluorescence separately for the dots as well as the homogeneous background on the flake. The resulting time traces are depicted in Figure S8 (b), the parameters extracted from biexponential fitting are listed in the main body, Table 1. Here, the homogeneous part of the PO/hBN3 hybrid is dominated by the ≈ 3 ns decay associated with unquenched monomer PO. The fluorescence from the bright
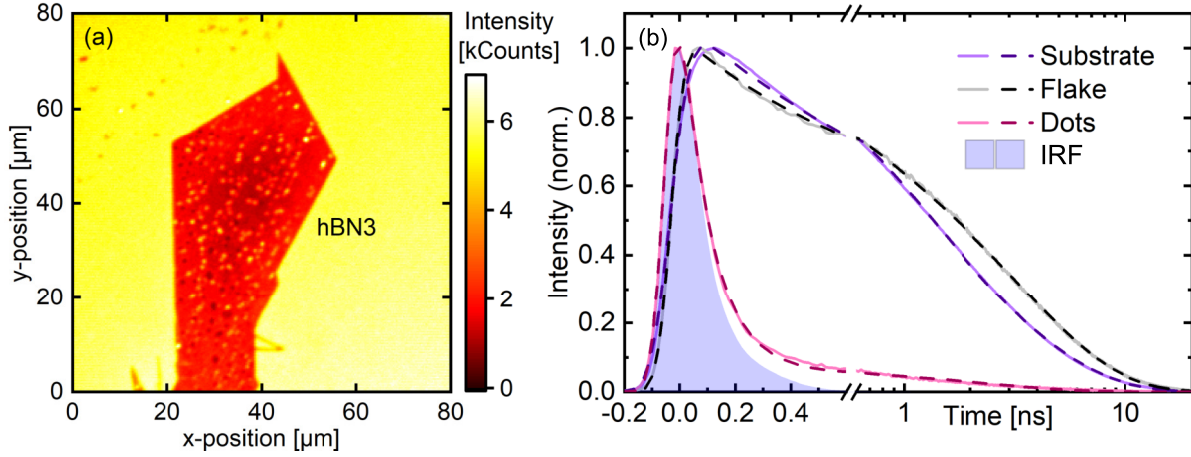
Figure S8: FLIM measurements of PO/hBN3. (a) Intensity map of PO-coated hBN3 flake and its surroundings. While the signal is homogeneous on the wafer, bright dots stand out from the flake area. In between these spots, the intensity grows only gradually from the inner region towards the rim. (b) Time traces from the different areas from (a). While for the substrate and the homogeneous part of the flake, the signal is long-living, it rapidly decreases at a similar speed as the IRF on the dots. Experimental data is depicted as pale and solid, fits as dark and dashed lines.

spots, however, essentially falls with the shape of the IRF, leaving merely a minor long-term contribution to the signal. We conclude that in the vicinity of the agglomerates, the excitons created upon pump absorption get quickly trapped in lower-lying excimer states, that emit light further in the red[6], which is barely transmitted by the bandpass filter (see section 1). The slow component of the decay may originate from the blue tail of this broad excimer emission or from monomer PO that resides too far from the relatively small agglomerates to get quenched by them but still resides and emits in the relatively large probe spot.

Given the variety in the size or brightness of the dots, we presume the existence of smaller agglomerates even on our standard samples. Note that due to their inherent quenching mechanism, this accumulation of dye will not result in an increase in fluorescence intensity until there is such a high number of molecules that their residual emission in the spectral range from 500 to 550 nm exceeds the monomer fluorescence of the surrounding homogeneous PO coating. Ergo, agglomerate formation will manifest in the time traces to start with. This explains the biexponential character of the monomer PO fluorescence decay on all hBN flakes. Additionally, these findings provide an approach to account for the different behavior of the hBN1 and hBN2 samples. The varying fluorescence intensity and contribution of the fast decay probably originate from slightly fluctuating molecule coverage in combination with different surface qualities of the two flakes, resulting in the formation of more or less agglomerates.

4.3 FLIM data of remaining flakes

In this part, we present the intensity maps for the remaining samples, whose relative intensities were analyzed in the main body, in the section "Rapid fluorescence quenching in TMDC hybrids". They were acquired with the same parameters, including the use of the band pass filter. The FLIM maps as well as the corresponding micrographs are depicted in Figure S9. Like for the hBN1 and WSe$_2$ flakes, we observe only a weak contrast between the insulating hBN flakes and their surroundings, while on the TMDC crystals, the fluorescence intensity of the PO is drastically reduced by up to three orders of magnitude. This demonstrates the quenching of the dye emission due to the charge or energy transfer from the excited molecules towards the underlying TMDC. Note that for the 1L-WS$_2$ flake, there is still some remaining signal from the monolayer photoluminescence transmitted by the filter.
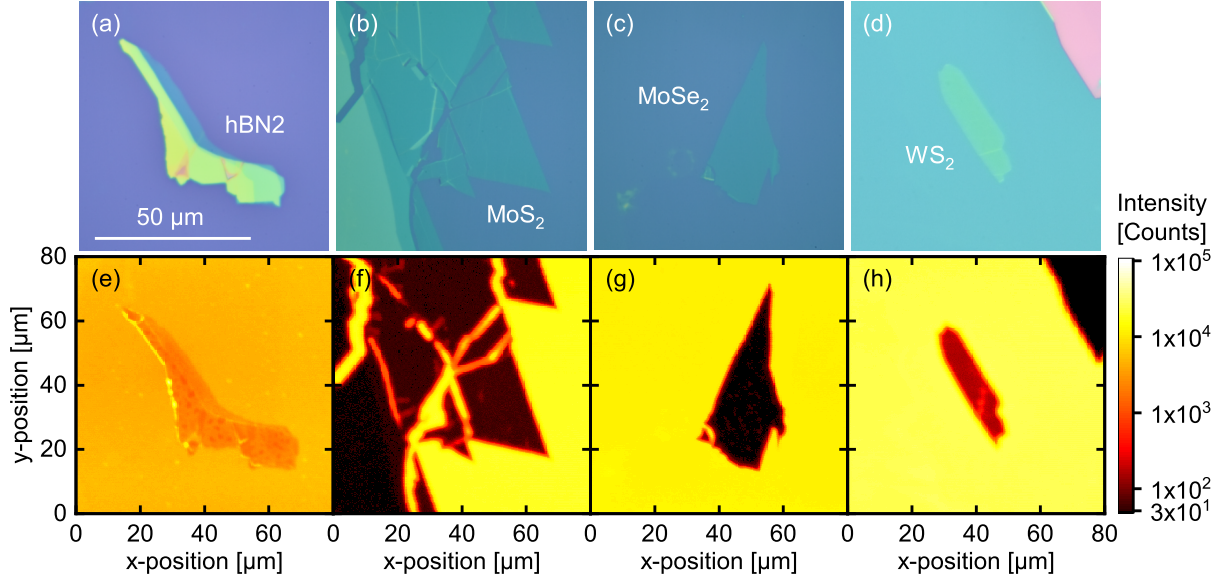
Figure S9: FLIM measurements of remaining hybrid structures. (a-d) Micrographs of hBN and 1L-TMDC flakes. (e-h) FLIM intensity maps of the regions depicted in (a-d). While for the hBN sample, the intensity difference between substrate and flake is comparably small, it exceeds two orders of magnitude in case of all the TMDCs. The intensity values from these measurements were used to calculate the quenching as shown in Figure 4 of the main body, while the corresponding time traces appear in Figure 5.

4.4 FLIM measurements without band pass filter

As mentioned in the main body, the advantages of the band pass filter are the exclusion of the 1L-TMDC photoluminescence as well as of the PO excimers or other agglomeration species. Here, we present an exemplary measurement on the WS_2 flake without the filter, see Figure S10 (a) and (b). Unlike in the filtered case, the TMDC flake stands out with a much higher intensity here, as the 1L photoluminescence is even stronger than the dye emission. Consequently, the detected intensity ratio does not relate to the quenching of the fluorescence anymore. This can also be
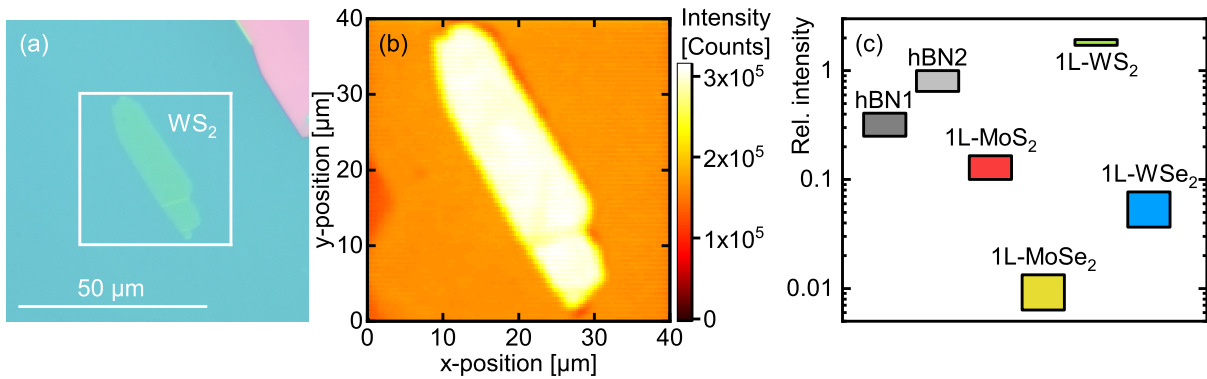

Figure S10: FLIM measurements without band pass filter. (a) Micrograph of the investigated WS_2 flake. The white square marks the area shown in (b). The flake is identical to Figure S9 (d). (b) FLIM intensity map of the area depicted in (a). In contrast to the measurements using a band pass filter, the flake clearly stands out brighter than its environment. (c) FLIM intensities on the different 2D material flakes relative to the respective substrate surroundings. Unlike for the filtered measurements, the intensities for the various TMDCs significantly differ from each other, with the 1L-WS_2 even exceeding the signal strength on the hBN flakes as well as the substrate. Generally, the relative intensities are higher than for the measurements using the filter.

deduced from Figure S10 (c), where the relative intensities of various flakes are compared. The TMDC intensities follow the same pattern as in the FLIM characterization before the molecule deposition, suggesting that those signals mostly originate from the flakes' photoluminescence. Ergo, the analysis of time traces would not yield any further information, as it would only show the decay of the TMDC-PL caused by exciton recombination, on a timescale of some 10 ps or even below[30–32], which hardly reaches the time resolution of these measurements.

4.5 Polarization-dependence of the fluorescence

Despite its function as a reference, we additionally used the hBN1 sample for polarization-dependent measurements, to trace any orientation preferences of the molecules relative to the hexagonally structured hBN surface. To that end, we kept the linear polarization of the excitation light fixed and rotated the wafer for consecutive scans. We then compared the intensity ratio between the (unordered) wafer substrate and that on the hBN between the different orientations. Statistical uncertainties arise from focus readjustments before each scan as well as the laser power fluctuations. Eventually, as demonstrated in Figure S11 (b), no systematic behavior was found, especially none with the expected periodicity of 60°. Au contraire, the ratio rather fell with the number of scans performed (Figure S11 (a)), pointing to a successive degradation of the molecules that proceeds faster on the hBN than on the wafer. Interestingly, the sharpest drop occurred during the 24-hour break between scan seven and eight, in which the sample was exposed to no laser light.
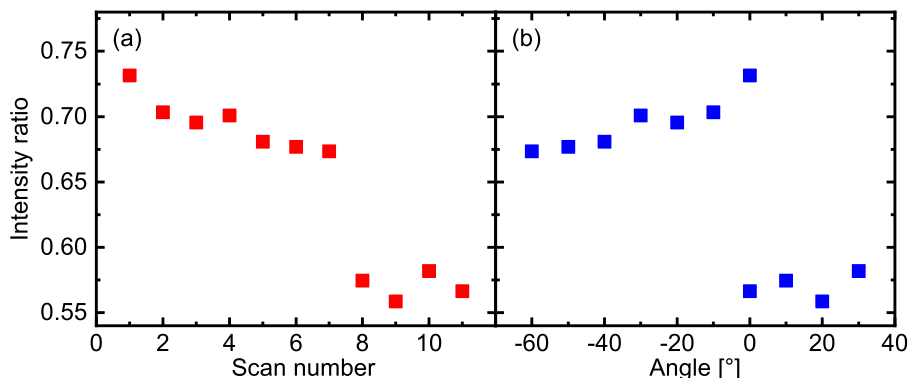

Figure S11: Investigation of polarization dependence of dye emission on the hBN1 flake in terms of the FLIM intensity ratio between flake and wafer plotted over (a) the temporal scan order and (b) the angle of the sample's in-plane orientation. (a) The intensity falls over time. Note that the change from scan seven to scan eight corresponds to a time span of one day, in which the measurements were interrupted. (b) No systematic dependence on the orientation angle ist observed. Especially the two measurements at 0° show that the changes over time dominate versus any potential polarization behavior.

References

[1] R. F. Fink, J. Seibt, V. Engel, M. Renz, M. Kaupp, S. Lochbrunner, H.-M. Zhao, J. Pfister, F. Würthner and B. Engels, *Journal of the American Chemical Society*, 2008, **130**, 12858–12859.

[2] D. Schmidt, M. Stolte, J. Süß, A. Liess, V. Stepanenko and F. Würthner, *Angewandte Chemie International Edition*, 2019, **58**, 13385–13389.

[3] Y. Shen, Z. Zhang, H. Liu, Y. Yan, S. Zhang, B. Yang and Y. Ma, *The Journal of Physical Chemistry C*, 2019, **123**, 13047–13056.

[4] R. D. Pensack, R. J. Ashmore, A. L. Paoletta and G. D. Scholes, *The Journal of Physical Chemistry C*, 2018, **122**, 21004–21017.

[5] Y. J. Bae, D. Shimizu, J. D. Schultz, G. Kang, J. Zhou, G. C. Schatz, A. Osuka and M. R. Wasielewski, *The Journal of Physical Chemistry A*, 2020, **124**, 8478–8487.

[6] A. L. Bialas and F. C. Spano, *The Journal of Physical Chemistry C*, 2022, **126**, 4067–4081.

[7] G. Seybold and G. Wagenblast, *Dyes and Pigments*, 1989, **11**, 303–317.

[8] F. Würthner, *Chem. Commun.*, 2004, 1564–1579.

[9] A. Castellanos-Gomez, M. Buscema, R. Molenaar, V. Singh, L. Janssen, H. S. J. van der Zant and G. A. Steele, *2D Materials*, 2014, **1**, 011002.

[10] J. Lub, P. A. van Hal, R. Smits, L. Malassenet, J. Pikkemaat and R. A. Hikmet, *Journal of Luminescence*, 2019, **207**, 585–588.

[11] D. Nečas and P. Klapetek, *Open Physics*, 2012, **10**, year.

[12] H. Lüth, *Solid Surfaces, Interfaces and Thin Films*, Springer Berlin Heidelberg, 2010, pp. 67–131.

[13] D. Wickramaratne, L. Weston and C. G. V. de Walle, *The Journal of Physical Chemistry C*, 2018, **122**, 25524–25529.

[14] J. Wilson and A. Yoffe, *Advances in Physics*, 1969, **18**, 193–335.

[15] M. M. Benameur, B. Radisavljevic, J. S. Héron, S. Sahoo, H. Berger and A. Kis, *Nanotechnology*, 2011, **22**, 125706.

[16] H. Li, G. Lu, Y. Wang, Z. Yin, C. Cong, Q. He, L. Wang, F. Ding, T. Yu and H. Zhang, *Small*, 2012, **9**, 1974–1981.

[17] D. den Boer, M. J. J. Coenen, J. A. A. W. Elemans and S. Speller, *Encyclopedia of nanoscience and nanotechnology*, American Scientific Publishers, Stevenson Ranch, Calif, 2nd edn, 2011, vol. 22.

[18] J. M. MacLeod and F. Rosei, *Small*, 2013, **10**, 1038–1049.

[19] S. J. Stranick, M. M. Kamna and P. S. Weiss, *Science*, 1994, **266**, 99–102.

[20] P. Matvija, F. Rozboril, P. Sobotík, I. Ošt'ádal and P. Kocán, *The Journal of Physical Chemistry Letters*, 2017, **8**, 4268–4272.

[21] C. Paris, A. Floris, S. Aeschlimann, J. Neff, F. Kling, A. Kühnle and L. Kantorovich, *Communications Chemistry*, 2018, **1**, year.

[22] S. Koslowski, D. Rosenblatt, A. Kabakchiev, K. Kuhnke, K. Kern and U. Schlickum, *Beilstein Journal of Nanotechnology*, 2017, **8**, 1388–1395.

[23] Z. Wang, R. Li, C. Su and K. P. Loh, *SmartMat*, 2020, **1**, year.

[24] Q. Cao, F. Grote, M. Huβmann and S. Eigler, *Nanoscale Advances*, 2021, **3**, 963–982.

[25] F. Zhang, Y. Ma, Y. Chi, H. Yu, Y. Li, T. Jiang, X. Wei and J. Shi, *Scientific Reports*, 2018, **8**, year.

[26] J. Jadczak, M. Glazov, J. Kutrowska-Girzycka, J. J. Schindler, J. Debus, C.-H. Ho, K. Watanabe, T. Taniguchi, M. Bayer and L. Bryja, *ACS Nano*, 2021, **15**, 19165–19174.

[27] E. Courtade, M. Semina, M. Manca, M. M. Glazov, C. Robert, F. Cadiz, G. Wang, T. Taniguchi, K. Watanabe, M. Pierre, W. Escoffier, E. L. Ivchenko, P. Renucci, X. Marie, T. Amand and B. Urbaszek, *Physical Review B*, 2017, **96**, 085302.

[28] E. Liu, J. van Baren, C.-T. Liang, T. Taniguchi, K. Watanabe, N. M. Gabor, Y.-C. Chang and C. H. Lui, *Physical Review Letters*, 2020, **124**, 196802.

[29] M. Yang, L. Ren, C. Robert, D. V. Tuan, L. Lombez, B. Urbaszek, X. Marie and H. Dery, *Physical Review B*, 2022, **105**, 085302.

[30] D. Lagarde, L. Bouet, X. Marie, C. R. Zhu, B. L. Liu, T. Amand, P. H. Tan and B. Urbaszek, *Physical Review Letters*, 2014, **112**, 047401.

[31] E. A. A. Pogna, M. Marsili, D. D. Fazio, S. D. Conte, C. Manzoni, D. Sangalli, D. Yoon, A. Lombardo, A. C. Ferrari, A. Marini, G. Cerullo and D. Prezzi, *ACS Nano*, 2016, **10**, 1182–1188.

[32] T. Völzer, F. Fennel, T. Korn and S. Lochbrunner, *Physical Review B*, 2021, **103**, 045423.